# Inorganic Nanotube Mesophases Enable Strong Self-Healing Fibers

*Won Jun Lee,[†‡] Erwan Paineau,[§] David Benbow Anthony,[†] Yulin Gao,[†] Hannah Siobhan Leese,[†¥] Stéphan Rouzière,[§] Pascale Launois,[§] and Milo Sebastian Peter Shaffer[†◊*]*

† Department of Chemistry, Imperial College London, South Kensington Campus, London, U.K. SW7 2AZ

§ Laboratoire de Physique des Solides, UMR CNRS 8502, Université Paris Sud, Université Paris Saclay, Bâtiment 510, Orsay, Île-de-France, FR 91405, France

◊ Department of Materials, Imperial College London, South Kensington Campus, London, U.K. SW7 2AZ

**Present Addresses**

‡ Department of Fiber System Engineering, Dankook University, Jukjeon, Yongin, Gyeonggi-do, KR 16890

¥ Department of Chemical Engineering, University of Bath, Claverton Down, Somerset, Bath, U.K. BA2 7AY

**Corresponding Author**

*E-mail: m.shaffer@imperial.ac.uk.

**Abstract**

The assembly of one-dimensional nanomaterials into macroscopic fibers can improve mechanical as well as multifunctional performance. Double-walled aluminogermanate imogolite nanotubes are geo-inspired analogs of carbon nanotubes, synthesized at low temperature, with complementary properties. Here, continuous imogolite-based fibers are wet-spun within a polyvinyl alcohol matrix. The lyotropic liquid crystallinity of the system produces highly aligned fibers with tensile stiffness and strength up to 24.1 GPa (14.1 N tex$^{-1}$) and 0.8 GPa (0.46 N tex$^{-1}$), respectively. Significant enhancements over the pure polymer control are quantitatively attributed to both matrix refinement and direct nanoscale reinforcement, by fitting an analytical model. Most intriguingly, imogolite-based fibers show a high degree of healability *via* evaporation induced self-assembly, recovering up to 44%, and 19% of the original fiber tensile stiffness and strength, respectively. This recovery at high absolute strength highlights a general strategy for the development of high-performance healable fibers relevant to composite structures and other applications.

**Keywords**

Exploiting the undoubtedly exceptional properties of individual nanostructures in macroscopic structures is often challenging. Anisotropic nanoparticles provide the load-transfer required for efficient mechanical reinforcement, however, they must be aligned, at high loading, without agglomeration, within a matrix. High strength fibers are an ideal context to develop nanocomposite systems, since they can be explored with modest quantities of material, whilst providing an anisotropic environment with a preferred orientation and loading direction. Fibers represent the state-of-the-art of high specific strength materials and are combined with resins to

produce high performance composite structures in a wide range of applications. Nanocomposite fibers provide an extra level of structural hierarchy, reminiscent of many natural materials, such as wood or bone. Mechanical efficiency in such fibers not only depends on the type of nanoreinforcement, including aspect ratio, length, surface chemistry/interfacial properties and intrinsic stiffness/strength, but also on the fiber microstructure including the matrix crystallinity and orientation of the constituents.[1]

One dimensional (1D) nanofillers are particularly well-suited to reinforce structural fibers, since they match the dimensionality, can pack efficiently, and can offer high aspect ratios. Carbon nanotubes have been widely used to reinforce composites/fibers, motivated by their high (specific) strength and stiffness, and other functional properties.[2] Promising fibers have been produced *via* a number of techniques,[3] including both dry[4] and wet coagulation spinning.[5] By wet-spinning from nematic liquid crystalline phases of single-walled carbon nanotubes (SWCNTs) in superacids,[2, 6] dense and highly ordered fibers have been produced with an exceptional balance of high strength and electrical/thermal conductivity.[2, 7]

Molecular liquid crystalline phases are widely used to spin commercial aramid and pitch derived carbon fibers, in order to maximize alignment. Liquid crystals (LC) are meso-morphic ordered states of anisotropic molecules or particles in solvents that bear liquid-like fluidity as well as a degree of crystal-like ordering;[8] a wide variety of such phases have been observed, including in DNA,[9] rod-like virus,[10] amphiphilic polymer,[11] and nanorod systems.[12] In principle, a range of such systems might be adapted to spinning functional fibers. Whilst carbon nanotubes offer many attractive properties, they require high synthesis temperatures, have relatively poor interfacial properties due to their graphitic surface chemistry, and can be difficult to process. Alternative inorganic 1D systems with similar dimensions are known, including some which occur naturally

due to geological processes, such as imogolite nanotubes.[13] Imogolite-related nanotubes are more readily manipulated than carbon systems, and offer complementary properties, including transparency, oxidation resistance and intrinsically stronger matrix binding. "Geo-inspired" synthetic versions of (substituted/doped) imogolites, but also of other sulfide, hydroxide, phosphate, and polyoxometalate nanotubes, are now available with well-defined morphologies.[14]

Recently, a liquid crystal columnar phase has been discovered in dilute aqueous suspensions of aluminosilicate and aluminogermanate imogolite nanotubes (INTs).[15] The existence of a lyotropic liquid crystal (LLC) phase at low concentration is attributed to strong Coulombic repulsion between high aspect ratio INTs. The INT structure can be described with a three-dimensional $(HO)_3Al_2O_3Si(Ge)OH$ elementary unit arranged in a rolled hexagonal lattice, with hydroxyl groups terminating both the exterior and interior wall.[16] INTs are inorganic analogs of carbon nanotubes,[17, 18] with similar dimensions, but the advantage that they are synthesized at low temperatures (around 100 °C).[19] INTs can respond to external stimuli and to different environments, and can be aligned, for example, *via* electric fields[15, 20] or physical deformation.[21] The mechanical properties of INTs, though lower than those of SWCNTs, are still predicted to be significant,[22] with a modulus on the order of 300 GPa. INTs are highly soluble in water and have the potential to form strong interfaces with suitable matrices through their densely hydroxylated surface. INTs have been used as a stiff, strong reinforcement in a variety of polymers to form composites,[23-27] and recently electrospun networks,[28] but the opportunities for continuous INT-based (composite) fibers have not yet been explored. Moreover, the electrospinning experiments were limited to an imogolite content no greater than 2 wt.%. In this study, we combine synthetic double-walled aluminogermanate INTs (DW Ge-INTs) with polyvinyl alcohol (PVOH), to wet-spin imogolite composite monofilament fibers, at high loadings. PVOH is a water-

processible polymer which is widely used for wet-spun nanocomposite fiber production,[5, 29-32] including with 1D fillers such as carbon nanotubes and nanocellulose. We chose these constituents, as a convenient model system, because lyotropic mesophase formation has been previously observed in PVOH/INT mixtures,[33] and the materials were expected to be highly compatible through hydrogen-bonding.

**Results and Discussion**

**Characterization of Double-Walled Aluminogermanate Imogolite Nanotube Composite Fiber Dope**

Established sol-gel methods[13] were used to synthesize DW Ge-INTs with mono-dispersed external diameters ca. 4.3 nm, and lengths around 85 nm with some INTs showing lengths up to 500 nm[13, 15] (Figure S1); a high aspect ratio is preferred for efficient reinforcement in composite fibers[34] and to encourage LC self-organization.[15] In dilute aqueous DW Ge-INT suspensions (volume fraction, $\phi_{DW\ Ge\text{-}INT} = 0.26\%$), mesophase formation was observed by polarized optical microscopy (POM), Figure 1 (a) in agreement with previous small-angle X-ray scattering data.[15]
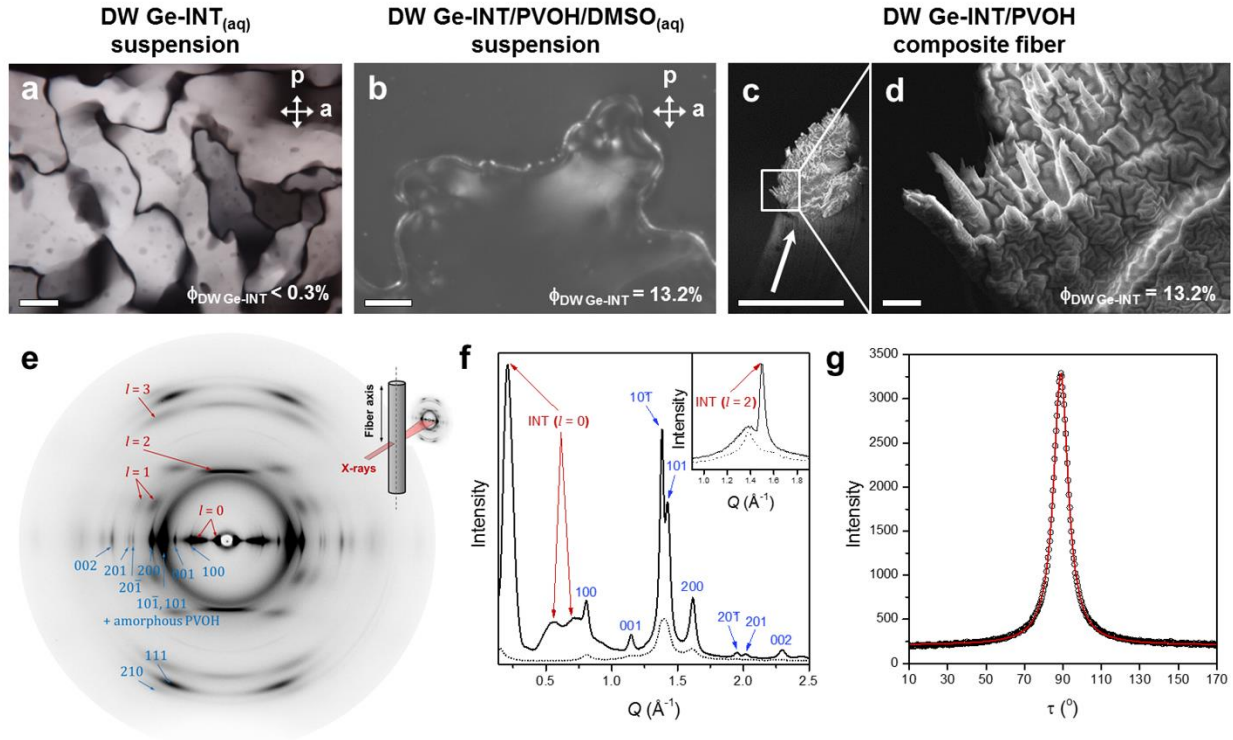
**Figure 1** (a) An aqueous suspension of DW Ge-INT under cross-POM ($\phi_{\text{DW Ge-INT}}$ = 0.26%), textured photograph displaying a hexagonal columnar liquid-crystal (ColH) phase, 200 μm scale bar. (b) Spinning dope (DW Ge-INT in PVOH/DMSO aqueous) suspension under cross-POM, optical micrograph textures of a mixture which exhibits a mesophase formation, 20 μm scale bar. (c) SEM cryofractured cross-section of a wet-spun DW Ge-INT/PVOH composite fiber with the white arrow indicating fiber axis (note that the cross-section is not perpendicular in relation to the fiber axis here), 50 μm scale bar, and (d) a higher magnification image, 2 μm scale bar. (e) A 2D WAXS pattern of wet-spun DW Ge-INT/PVOH composite fiber ($\phi_{\text{DW Ge-INT}}$ = 3.8%), the fiber axis is vertical and the incident beam is perpendicular to the fiber axis as shown in the sketch; red arrows indicate nanotube contribution (located in planes $l*2\pi/T$ perpendicularly to the nanotube axes, $T \approx 8.5$ Å is the period along the nanotube) and blue arrows indicate PVOH scattering features (the hkl integers in blue index peaks of crystalline PVOH). (f) The corresponding WAXS diagram along a horizontal line passing through the center of the image in (e). The solid line is the

signal from the composite fiber ($\phi_{\text{DW Ge-INT}} = 3.8\%$) and the dotted line from a PVOH fiber ($\phi_{\text{DW Ge-INT}} = 0\%$) taken in the same configuration. The inset corresponds to a scan in the perpendicular direction, *i.e.* along the fiber axis. (g) Experimental (open circles) and fitted (red curve) azimuthal profiles of the scattered intensity at Q = 0.6 Å$^{-1}$.

**Composite Fiber Dope Characterization**

To prepare solutions (dopes) for spinning, DW Ge-INTs were added to a PVOH/dimethyl sulfoxide (DMSO) aqueous solution at ca. 1, 10, 20 and 30 wt.%, corresponding to 0.4, 3.8, 8.1 and 13.2 vol.% ($\phi_{\text{DW Ge-INT}}$), respectively. DMSO was chosen as the primary solvent as it more readily dissolves PVOH than water and reduces the temperatures required for processing.[35] Polarized optical microscopy (POM) showed that, at low DW Ge-INT volume fractions ($\phi_{\text{DW Ge-INT}} \leq 3.8\%$), the mixtures remain isotropic without any mesophase formation, similar to the PVOH control (100 wt.% PVOH), Figure S2. However, above 8.1 vol.% DW Ge-INTs, birefringent domains indicate a two-phase composition of anisotropic, liquid crystal like, and DW Ge-INT domains coexisting with isotropic regions, Figure 1 (b) and Figure S2 (d), (e). The initially clear solutions of PVOH and INT, maintained clarity on mixing; the optical microscopy, showing birefringence and no scattering, rules out large scale aggregation in the dopes.[33]

Composite fibers were wet-spun and drawn from the DW Ge-INT PVOH/DMSO (aq) dopes (see Methods and Materials for detailed procedure). The resulting composite fibers were found to have predominately circular or ribbon-like profiles *via* scanning electron microscopy (SEM) (Figure 1 (c) and (d), full fiber series shown in Figure S3), and were dense without any apparent voids after hot-drawing. The nominal circular radius for the baseline PVOH fibers was ca. 20 μm. The DW Ge-INT/PVOH fibers had a nominal circular radius between 15-25 μm, with the slightly higher values for higher DW Ge-INT loading (data provided in Table S2, with

thermogravimetric analysis provided in Figure S4 and Figure S5). A high level of birefringence was observed for all fibers by POM (Figure S6), qualitatively indicative of well dispersed nano-reinforcement and high degrees of alignment within the microstructure.

The crystallinity and alignment of the PVOH matrix within the composite fibers influences the mechanical properties of the fibers.[35] Post-spinning conditioning is often performed by drawing at high temperatures close to PVOH melting point, but below the degradation temperature. Both molecular orientation with respect to the fiber axis and crystallinity increase with drawing temperature,[36] up to an optimum reported to be approximately 40 °C below the melting point.[37] In this study, the DW Ge-INT PVOH fibers were drawn at 180 °C (melting point ca. 226 °C) at a ratio of 1:10 (or 1:5 for $\phi_{DW\ Ge-INT}$ = 13.2%), to improve their mechanical properties. Contrary to observations in random PVOH/imogolite films,[23] differential scanning calorimetry (DSC) experiments (DSC) experiments (Figure S7, data provided in Table S1), showed that the addition of DW Ge-INT to the drawn fibers increased the degree of crystallinity of the PVOH component, from 21.6 wt.% crystalline in the pure polymer fiber, to 32.4 wt.% (50% increase) at $\phi_{DW\ Ge-INT}$ = 8.1%. At the highest loading, $\phi_{DW\ Ge-INT}$ = 13.2%, PVOH crystallinity dropped slightly to 27.2 wt.% likely due to the lower attainable draw ratio. The PVOH crystallinity is relatively low in all fibers, compared to maximum literature values (fibers containing PVOH only, ~55-68 wt.% crystallinity),[35, 36] due to the modest spinning parameters applied in these comparative experiments. With larger quantities of INTs, there is scope for optimizing the spinning parameters, for example through increasing dope concentration, reducing bath temperatures and by hot-drawing at higher temperatures. Nevertheless, the DW Ge-INTs clearly act as heterogeneous nucleation sites during the hot-drawing process (as observed for (modified) carbon nanotubes),[32, 38, 39] due to their enhanced alignment and/or compatible hydroxylated surface.

The alignment of both the DW Ge-INTs and the PVOH matrix was assessed by 2D Wide Angle X-ray Scattering (WAXS) in transmission (Figure 1 (e)). The intensities are modulated angularly, depending on the degree of orientation of each phase. Linear scans performed along two perpendicular directions of the WAXS pattern provide the scattering signal *I(Q)* at azimuthal angles $\tau = 0°$ and 90°, respectively parallel and perpendicular to the fiber axis (Figure 1 (e)). The scattering features can be indexed to crystalline PVOH and DW Ge-INTs (Figure 1 (e) and (f)). Crystalline PVOH has space group P2$_{1/m}$ with unit cell parameters *a* = 7.81 Å, *b* = 2.52 Å, *c* = 5.51 Å, and $\gamma$ = 91.7°.[40] The corresponding Bragg peaks are labelled by three Miller indices h, k and l, as usual. The average crystallite sizes (L), estimated by the Scherrer equation (tabulated in Table S4), are rather similar in both c* (L ~30 nm) and a* (L ~25 nm) directions, in good agreement with a commercial PVOH fiber reference (Kuralon 1239, L ~20 nm, Figure S9 and Table S4). For DW Ge-INTs, nanotube scattering is simply 'indexed' by an integer *l*. Since these DW Ge-INTs are periodic along their long axis, with period $T \approx$ 8.5 Å, their scattered intensity is located in reciprocal planes perpendicular to their long axis, at $Q_z = l\frac{2\pi}{T}$, with *l* integer.[16, 41] The scattered intensity below *Q* < 0.8 Å$^{-1}$ lies in the equatorial plane *l* = 0, and displays large oscillations characteristic of the squared form factor of double-walled nanotubes without any positional ordering[13] (Figure 1 (e)). Specifically, the three strong intensity maxima (indicated with red arrows in Figure 1(f)) match those observed for DW Ge-INTs diluted individually in suspension (refer to Fig. 1 in Amara *et al.*).[13] The DW Ge-INTs (which are monodispersed in diameter) do not form bundles within the fibers; if they did, the intensity would be the convolution of this square form factor with the structure factor of the corresponding bidimensional lattice.[42, 43] The *l* = 0 intensity is maximum for $\tau$ = 90° (Figure 1 (f)), indicating that DW Ge-INTs are preferentially aligned along the fiber axis. The most intense scattering signal from amorphous PVOH is located around 1.4 Å$^{-}$

[1], corresponding to the inter-chain distance in amorphous PVOH. However, the $10\bar{1}$ and 101 peaks of crystalline PVOH appear at around the same spacing, with the chains aligned along the $\vec{b}$ axis of the unit cell.[44] These amorphous and crystalline signals are maximum for $\tau = 90°$, perpendicularly to the fiber axis, showing that the PVOH chains are preferentially oriented along the fiber axis, like the DW Ge-INTs.

The degree of alignment can be quantified using the orientation order parameter, based on formalism developed previously for SWCNT fibers[45] and detailed in the Supporting Information. The angular distribution of the Ge-INT and PVOH scattering features at $Q = 0.6$ and $1.4$ Å$^{-1}$ can be fitted to a Lorentzian distribution (example in Figure 1 (g) for $\phi_{DW\ Ge-INT} = 3.8\%$, other fits in Figure S8). Orientation distribution probability in real space is deduced from the angular distribution in reciprocal space. The corresponding order parameters $S = <\frac{3cos^2(\theta)-1}{2}>$ can be derived for both DW Ge-INTs and PVOH, where $\theta$ is the angle between the fiber axis and nanotube or PVOH chain axes (Table S3). Due to the overlap of the diffuse amorphous peak of PVOH with the $10\bar{1}$ and 101 crystalline peaks, a single, combined PVOH orientation parameter was determined. PVOH orientation increased strongly on adding DW Ge-INT, from $S = 0.5$ in the pure polymer fiber to $S \approx 0.9$ for $\phi_{DW\ Ge-INT} = 0.4$, 3.8 and 8.1%. However, at $\phi_{DW\ Ge-INT} = 13.2\%$, the alignment of both the nanoreinforcement and matrix began to decline, to $S = 0.83$, and $\leq 0.7$ for the DW Ge-INT and PVOH matrix, respectively. As discussed further in the Supporting Information, in this case, the polymer alignment appears to become bimodal, consistent with the onset of disordered segregation of the DW Ge-INTs.

**Tensile Properties of Composite Fibers**

The continuous composite fibers were collected, an example is shown in Figure 2 (b), and then sampled for mechanical characterization. The tensile properties were normalized by linear density to give values in (N tex$^{-1}$), which is conventional for textile fibers, as it avoids errors due to uncertain fiber diameters, particularly for non-circular cross-sections. For comparison with other nanomaterial studies, however, these values were converted to strengths (GPa) using the fiber average cross-sectional areas deduced from the ratio of the measured linear density and calculated bulk density, which were also consistent with measured cryofractured cross-sections (SEM). The linear densities for all composite fibers was between 1 and 4.5 tex (*i.e.* grams per kilometer of fiber). The mechanical property trends are consistent with both approaches, however area-normalized strength and stiffness values show larger relative improvements, since the DW Ge-INT have a significantly higher density (3.6 g cm$^{-3}$ for determination see Supporting Information) than the polymer (1.269 g cm$^{-3}$, 1.345 g cm$^{-3}$ for amorphous and crystalline PVOH, respectively).[46] Typical tensile stress-strain curves of wet-spun and hot-drawn composite fibers (Figure 2 (d) to (f) and Table S5) show that the addition of DW Ge-INTs increased the strength and stiffness of the composite fibers, for volume fractions 3.8% and 8.1%. At higher concentrations (13.2%), the addition of DW Ge-INT was less effective, as expected, given that the WAXS studies showed reduced alignment of the nanotubes and of the polymer with respect to the fiber axis and DSC indicated a lower degree of PVOH crystallinity. As is typical for nanoreinforced systems, the strain-to-failure reduced in all cases. All fibers showed a consistent stress-strain profile with an initial yield at 0.5% strain attributed to the yield of the amorphous PVOH component, common to all samples. The composite fiber with $\phi_{DW\ Ge-INT} = 8.1\%$ exhibited the highest stiffness (24.1 ± 1.8 GPa) and strength (794 ± 50 MPa), an increase of 143% and 30% compared to the pure PVOH

fiber ($\phi_{DW\ Ge\text{-}INT} = 0\%$) stiffness (9.9 ± 2.6 GPa) and strength (603 ± 71 MPa), respectively; on the other hand, the strain-to-failure reduced from ca. 9% to 5.5%. The increases are particularly significant, given the high absolute baseline of the matrix. However, depending on the polymer tacticity and processing parameters (drawing), the mechanical properties of pure PVOH fibers can vary significantly. Highly syndiotactic PVOH fibers (diad syndiotacticity 69%) with optimized processing can reach stiffness and strengths up to 38 GPa and 1400 MPa,[35] suggesting that further improvements with regards to matrix alignment/microstructure are possible. Qualitatively, the mechanical performance of the DW Ge-INT/PVOH fibers follows the trends observed in both matrix crystallinity and INT alignment. The key question of how much of the enhancement in the DW Ge-INT/PVOH fiber performance is due to direct reinforcement, rather than the polymer microstructure, can be addressed by comparison to (model) predictions.
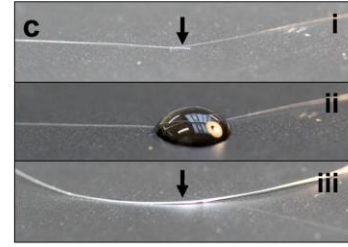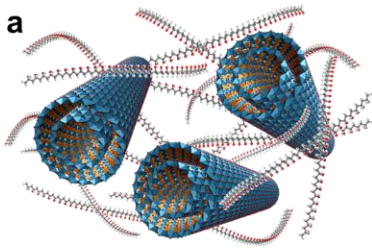
**Original DW Ge-INT reinforced PVOH composite fibers**
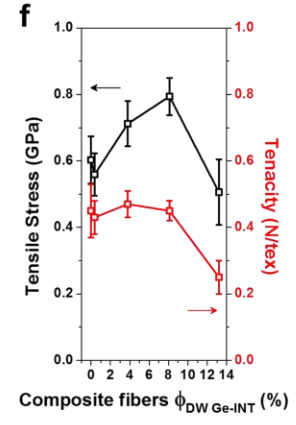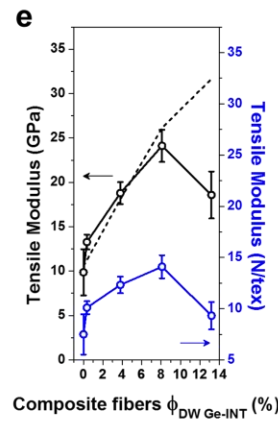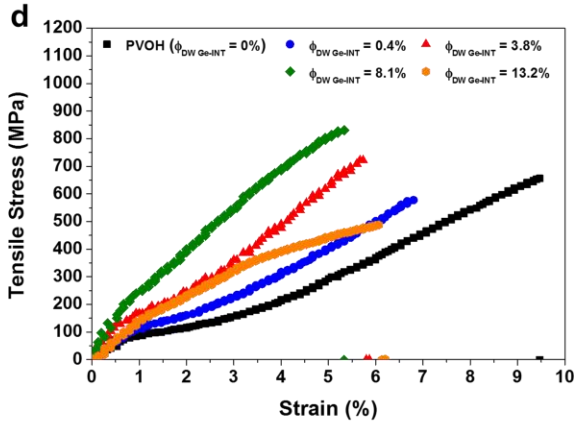


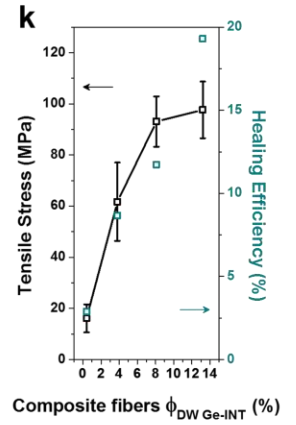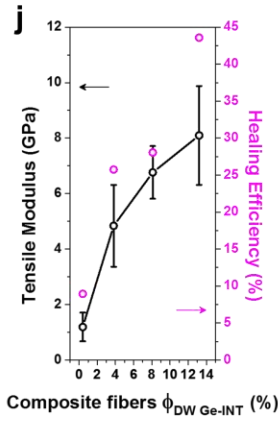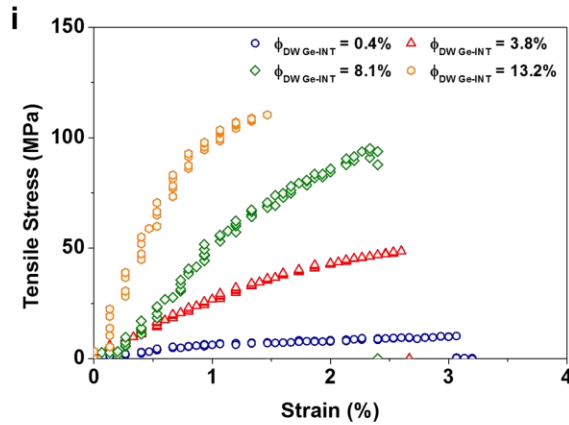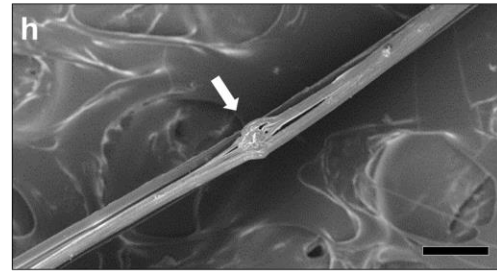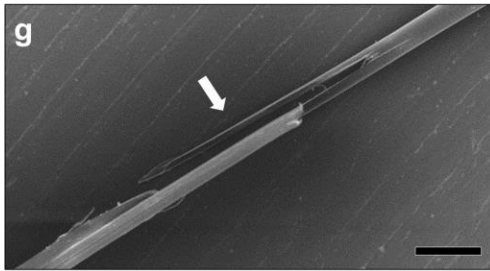**Healed DW Ge-INT reinforced PVOH composite fibers**

**Figure 2 (**a) A cartoon of DW Ge-INTs in a PVOH matrix. (b) A photograph of continuous wet-spun DW Ge-INT/PVOH composite fibers formed on a winder. (c) Photographs of the autonomic healing process; (i) a failed composite fiber, (ii) a heat droplet of water is pipetted onto the two fractured surfaces, (iii) the fiber is healed *via* an evaporation induced self-assembly process. The black arrow highlights the position of the break in the top and bottom image. (d)-(f) Mechanical properties of DW Ge-INT/PVOH composite fibers with a comparison to a PVOH fiber baseline, $\phi_{DW\ Ge-INT} = 0\%$. (d) Characteristic stress strain curves, (e) tensile modulus with a theoretical tensile modulus (from a modified Krenchel's model in GPa) depicted by a dashed line, and (f) tensile strength. Morphology and mechanical properties of EISA healed DW Ge-INT/PVOH composite fibers. (g) Scanning electron micrographs of composite fiber ($\phi_{DW\ Ge-INT} = 8.1\%$) after failure, and (h) after evaporation induced self-assembly healing process. A white arrow indicates a similar position before and after the process, 100 μm scale bar. (i) Characteristic stress-strain curves of healed fibers, (j) tensile modulus with healing efficiency as a percentage of original stiffness, and (k) tensile stress with healing efficiency as a percentage of original strength for healed DW Ge-INT/PVOH composite fibers. The PVOH fiber ($\phi_{DW\ Ge-INT} = 0\%$) could not be healed using the EISA procedure. The Imperial logo is used with permission from Imperial College London.

Krenchel's micromechanical model predicts stiffness using a rule of mixtures approach, modified to take account of orientation and finite length effects; by adding an additional term, the effects of varying matrix crystallinity can also be included (see Supporting Information for further details). There is excellent agreement between the predictions of the model and the experimental data, when applying known values for DW Ge-INT loading/length/alignment and PVOH crystallinity, as well as the moduli of the different components (see dotted line, Figure 2 (e));

notably, there are no additional free fitting parameters. The quality of the fit confirms a strong filler-matrix interaction and indicates, again, that the dispersion is excellent for the majority of the samples, only deviating at the highest loading fraction .The increase in tensile modulus for the majority of composite fibers can therefore be attributed to the high intrinsic stiffness of the DW Ge-INTs (328 GPa);[22] however, the increased PVOH crystallinity also contributes significantly. As an example, the Krenchel model predicts an increase in modulus from 10.6 to 26.1 GPa on increasing DW Ge-INT loading from $\phi_{DW\ Ge-INT} = 0\%$ (pure PVOH fiber) to $\phi_{DW\ Ge-INT} = 8.1\%$, respectively. This 15.5 GPa increase can be assigned as follows: +10.8 GPa (69.4%) due to the DW Ge-INT reinforcement, +5.6 GPa (36.2%) due to the increase PVOH crystallinity (20.6 vol.% to 35.8 vol.%), balanced by a reduced amorphous contribution of -0.9 GPa (-5.6%). The orientation of the PVOH is not included in the model, as not all the parameters are known; however, since the polymer order parameter is similar ($S_{PVOH} \sim 0.9$), across the range of stiffer nanocomposites, it is clear that the INT content and PVOH crystallinity are the key factors.

**Self-Healing High Strength Fibers**

Despite recent advances in self-healing hydrogels,[47] films,[48, 49] and composites,[50] high performance, self-healing fibers have yet to be produced. Polymer composite systems can have higher strengths, but so far only the matrix is healed, never the fibers, limiting the scope for repair.[50] Truly self-repairing structural materials, based on composites,[51] would require self-healing fibers, a particularly important yet challenging target. Typically, the highest performance structural fibers are based on glassy,[52] semi-crystalline,[53] or cross-linked polymers[54] that fail irreversibly, even when reinforced with stiff nano-materials.[5, 55] Whilst healable fibers have been reported, based on a carboxylated polyurethane matrix,[56] the absolute mechanical properties were very low before and after healing, on the order of a few MPa for tensile strength

and stiffness. A more promising route to produce a self-healing material, would combine a nanoreinforcement with a matrix that can reform dynamically in response to a suitable stimulus,[57] as demonstrated for adhesive films.[58] The INT fibers developed in the current study are promising possible prototypes that may be self-stiffening under dynamic stresses,[59] since with plasticization, the INT mesophase may provide a mechanism for self-organisation.[60]

Strikingly, the DW Ge-INT reinforced PVOH nanocomposite fibers show a significant degree of healability, at an exceptionally high absolute strength and stiffness, using water as a medium for self-healing. The process of evaporation induced self-assembly (EISA) was simple: a droplet of water was injected onto the fractured region of fiber and allowed to evaporate, allowing spontaneous associations to form an organized, repaired structure (Figure 2 (c) and Supporting Video S1, with snapshots before and after EISA shown in Figure 2 (g) and (h), respectively).[61] As PVOH is not mobile at room temperature, in this EISA procedure, the droplet was heated above the PVOH glass transition temperature ~80 °C to allow the system to relax. The healing aspect of the approach was strongly linked to the presence and concentration of DW Ge-INTs. Indeed, in the absence of DW Ge-INTs in the composite fiber ($\phi_{DW\ Ge-INT}$ = 0%), the EISA procedure did not fuse the fractured surfaces sufficiently for any further mechanical tests. Instead, internal relaxation of the aligned polymer caused the fibers to distort and contract away from contact (Figure S10). This response highlights the challenge of healing high performance fibers: excellent mechanical properties require aligned polymers, generally incompatible with the relaxation required for healing.

Given these difficulties, the mechanical properties of nanocomposite fibers recovered surprisingly well after healing (Figure 2 (i) to (k), individual stress-strain curves are shown in Figure S11 and tabulated properties available in Table S6). The maximum recovered stiffness

reached 8.1 GPa (16.2 N tex$^{-1}$) or 44% of the initial unbroken values, for the fiber with the highest nanofiller loading ($\phi_{\text{DW Ge-INT}}$ = 13.2%). In principle, the healed stiffness is, numerically, a function of gauge length, but the values demonstrate a functionally useful degree of repair. More importantly, the strength recovery was also significant (19%), with the maximum recovered strength again shown at highest loadings ($\phi_{\text{DW Ge-INT}}$ = 13.2%, 98 MPa (0.05 N tex$^{-1}$)). Qualitatively, POM (Figure 3) showed some disorder in the birefringence after healing, but a degree of alignment was retained in the previously fractured region. The failure mechanism for healed fibers was typically more brittle than the original fibers as expected given the presence of a defective region.
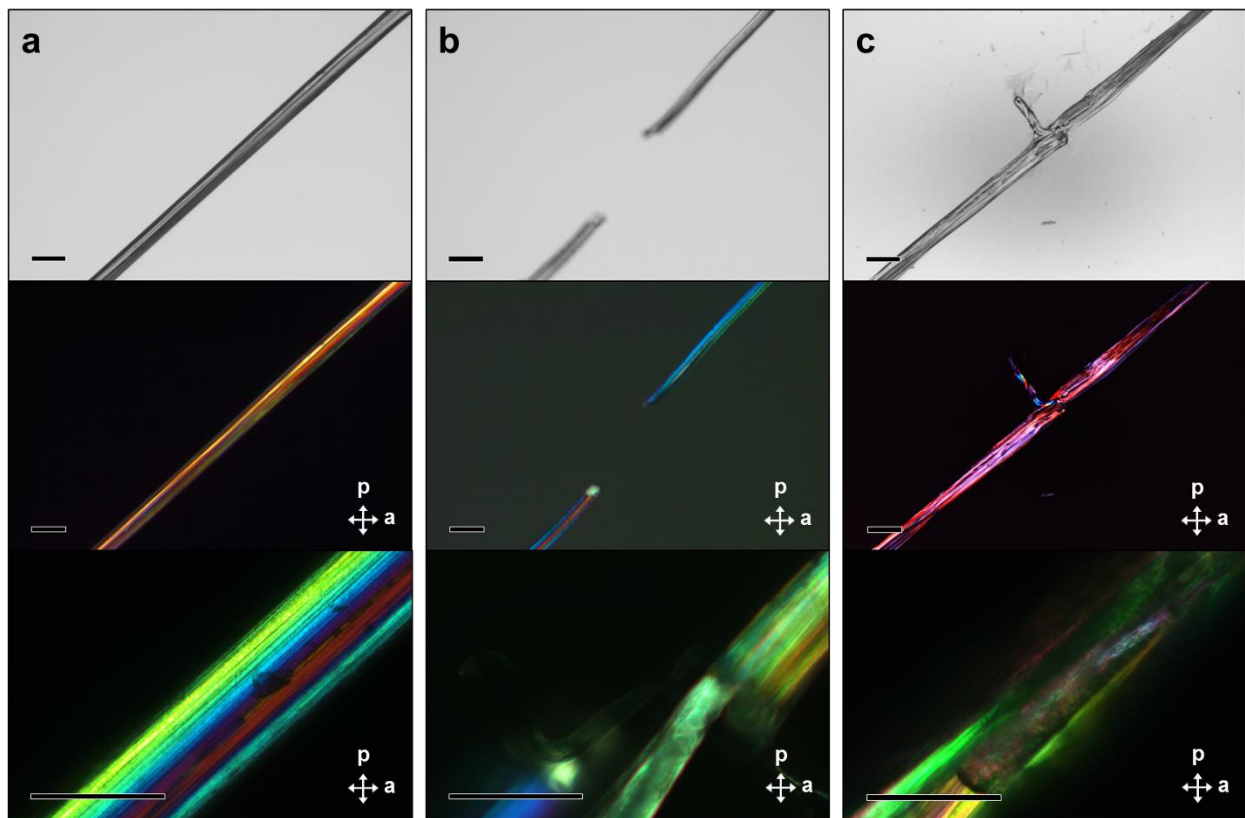


**Figure 3** Optical microscopy (top, without polarizers) and cross-POM (middle, 0°/90° and bottom, 0°/90° at higher magnification) micrographs showing the birefringence of a DW Ge-INT/PVOH

composite fiber ($\phi_{DW\ Ge-INT}$ = 8.1%), (a) before failure, (b) fractured fiber, and (c) healed fiber. 100 µm scale bar for all frames.

The DW Ge-INTs may enable the healing process by a number of mechanisms. Firstly, they form a higher surface area, fibrillated failure surface that is more rapidly softened by the water, and which provides greater overlap between the broken sections. At the same time, they provide a highly anisotropic scaffold that maintains the oriented fiber structure during the rearrangement of the polymer, and likely a template/nucleating surface for subsequent polymer recrystallisation. The 2D WAXS patterns (Figure S8) and the DSC data (Table S1) highlight the ability of the DW Ge-INTs to enhance oriented crystallization within the fibers. The small diameter of the DW Ge-INTs, on the order of the radius of gyration of the polymer, implies direct contact with the majority of PVOH molecules. Whilst the rheology of such colloidal rod systems is still under study, the long length of the DW Ge-INTs implies slow rotational relaxation.[62] The ability to form mesophases in dilute DW Ge-INT/PVOH solutions may also aid the EISA healing procedure, by encouraging and maintaining local alignment within the repair parallel to the undamaged oriented fiber structure, even when plasticized. The response is quite different to simple thermoplastic melting which does not preserve morphology or alignment. It is also different to many other self-healing systems that rely on a very soft mobile phase interpenetrating with a more rigid phase, since both the INT and the (re)crystallized PVOH are stiff and highly anisotropic.

While the healing efficiency can be high (80-100%), self-healing systems[55] based on hydrogels or supramolecular motifs have low mechanical properties (strengths < 1MPa;[58] stiffness ~10-100 MPa), and long recovery times (1 h to 24 h), due to the molecular inter-diffusion required.[47] Bulk thermoplastics can be remelted at temperature, but the lack of alignment limits strength to below 100 MPa, with poor shape control; reversibly cross-linked resins require elevated

temperatures for extended periods, and have intermediate properties;[63] autonomous liquid resin infused crack repair is challenging to implement due to the need to incorporate reactive monomers and the associated parasitic weight of capsules or vasculature.[50, 64] This latter type of self-healing fiber composite, only repairs the matrix, not the primary load-bearing reinforcements which remain unbroken. In general, there is an expected trade-off between the mechanical properties and the healing efficiency.[65] The healing of imogolite-based fibers can take place in relatively short time scales (t < 10 min) and at relatively low temperature (95 °C), with excellent absolute performance compared to all other systems. This healing process uses straightforward, benign conditions; there are no reactive monomers, no toxic solvents, and the temperature is well below that often used for structural composite repairs *in situ*, as well as below the boiling point of water where bubble formation could cause damage.[66] A comparison of the imogolite fibers with the tensile properties reported for other known self-healing materials (Figure 4) highlights their exceptional performance. There is general trend between initial tensile modulus and healed strength, following the usual relation between strength and stiffness observed in the well-known Ashby plots for material properties.[67] The INT-PVOH composite fibers extend the mechanical performance range of healable materials by two orders of magnitude, in tension, and demonstrate that it may be possible to produce structural fibers that are healable at the microscale component level. The potential to improve reliability and extend a material's lifetime through the use of smart textiles,[68] which can recover after an initial failure,[69, 70] is desirable in many applications including for composite materials, ropes/cords, wearable technologies, as well as environmentally responsive fabrics.[71] Whilst PVOH is a water-sensitive polymer, it is already used commercially, including in fiber form, with some less soluble grades marketed for reinforcement of concrete, mortars, and some thermoplastics, as well as components of ropes/cords. Interestingly, the addition

of DW Ge-INTs reduces water uptake very significantly, from around 60 wt.% to 5 wt.% after extended exposure (Figure S5), again highlighting the intimate interaction between nanofiller and matrix. This stabilization may broaden the applicability of PVOH fibers; however, there is also scope to develop the self-healing mechanism in other 1D nanofiller/matrix combinations, or to adapt imogolites to more hydrophobic matrices with suitable chemistry.[72, 73] From an economic standpoint, other geologically available materials, such halloysite nanotubes, may be relevant since they form interesting mesophases[74] and are available at low cost from abundant deposits worldwide.[75]
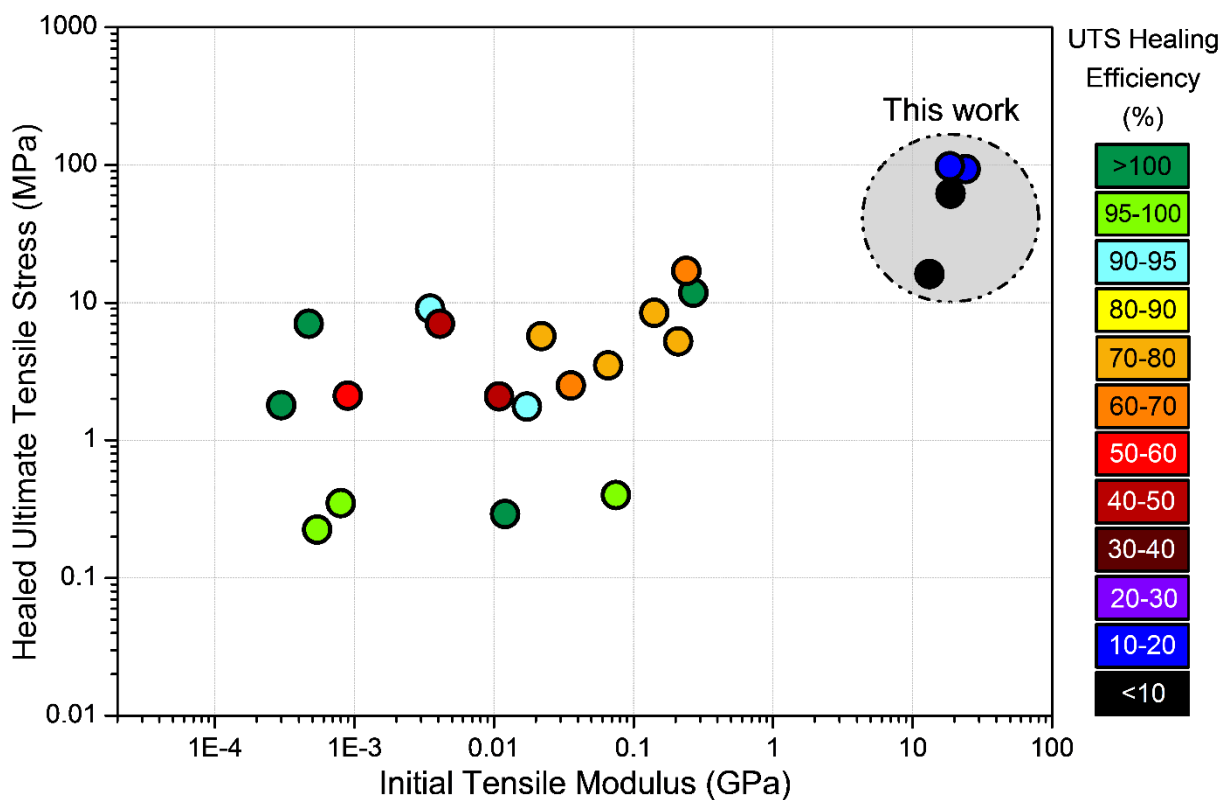


**Figure 4** Healed ultimate tensile stress (UTS) against initial tensile modulus for self-healing materials tested in pure tension, after complete failure. Data for DW Ge-INT/PVOH composite fibers tested here are highlighted within the circle. The filled colors for each point relate to the

healing efficiencies from initial to healed UTS. Tabulated literature values and their corresponding references are provided in the Table S7 and Table S8.

**Conclusions**

In summary, high performance, healable composite fibers were produced by reinforcing polyvinyl alcohol (PVOH) with double-walled aluminogermanate imogolite nanotubes (DW Ge-INTs). At higher DW Ge-INT concentrations in the fiber spinning dope, a biphasic liquid crystal formed, including anisotropic discrete DW Ge-INT domains. Nanocomposite fibers prepared by coagulation spinning from these dopes showed significant alignment (WAXS) of both constituents, DW Ge-INTs and PVOH, and increased PVOH crystallinity (DSC). These imogolite nanotube reinforced polymer fibers are conceptually analogous to the more widely studied carbon nanotube reinforced systems, whilst offering a different portfolio of properties, including transparency and oxidation resistance. Although the imogolite is crystalline, in composite terms, the system might loosely be described as a 'nano-glass' fiber version of 'nano-carbon' fiber reinforcements. The absolute mechanical performance of the fibers (24 GPa (14.1 N tex$^{-1}$) and 0.8 GPa (0.45 N tex$^{-1}$), respectively, with a strain-to-failure of 5.3%) is encouraging and consistent with other nano-reinforced PVOH studies. The DW Ge-INTs provide both direct reinforcement and matrix refinement, exploiting a convenient, colorless nanomaterial which can be synthesized at high yield, and wet-spun at room temperature, in aqueous environments. Most notably, the presence of the nanofiller allowed a significant proportion of the properties of the fiber to be recovered after fracture (up to ~44% and ~19% of the original tensile stiffness and strength, respectively, and 66% of the original strain-to-failure). Further improvements to this system are anticipated, for example using longer or more monodispersed DW Ge-INTs, as well as using a more crystalline polymer (for example, PVOH with controlled tacticity). Whilst healing of

relatively weak gels and isotropic resins has been demonstrated, the repair of high-performance fibers is much more challenging. This embodiment of a healable fiber, with performance in the structural range, provides a route towards fully self-healing composite structures, in which the primary fibers, not just the matrix, can be repaired. In principle, wet-spinning is a simple and scalable route, widely used for high performance fibers, including polyaramids, such as Kevlar, and PAN precursors for carbon fiber. The fundamental strategy established in this paper is worthy of further mechanistic study, and may be developed broadly using other nano-reinforced fiber systems to improve performance, cyclability, and environmental tolerance, towards a range of applications.

## Methods and Materials

The imogolite nanotubes were synthesized using aluminum perchlorate nonahydrate (ACS reagent, $\geq$ 98%), and tetraethoxygermanium (TEOG, $\geq$ 99.95%) in urea ($CO(NH_2)_2$, ACS reagent, 99%). The matrix used for the composite fibers was polyvinyl alcohol (PVOH, Mowiol 56-98, MW ~195,000, 98.0-98.8 mol% hydrolysis, Kuraray Co. Ltd, JP), which was used in the composite fiber dope when dissolved into dimethyl sulfoxide (DMSO, ACS reagent, $\geq$ 99.9%), purchased from Sigma Aldrich, GB. The coagulation bath solution for fiber production contained acetone (99.5% GPR RECTAPUR) purchased from VWR, GB.

## Synthesis and Characterization of DW Ge-INT

Double-walled aluminogermanate imogolite nanotubes (nominal formula $(HO)_3Al_2O_3GeOH$, DW Ge-INT) were synthesized using a single-step process, as described in detail elsewhere.[13] Typically, the synthesis consists in the co-precipitation of TEOG with a dilute (C = 0.2 mol $L^{-1}$) aluminum perchlorate solution in a Teflon beaker using the imogolite stoichiometric ratio [Al]/[Ge] = 2. Then, a urea solution was added at room temperature up to a

[urea]/[Al] ratio of 1. The thermal decomposition of urea produces *in situ* hydroxyl ions (two hydroxyls per urea molecule) homogeneously distributed in the solution. Immediately after mixing, the solution was transferred into an autoclave and placed in an oven at 140 °C for 5 days. After hydrothermal synthesis, the DW Ge-INT suspension was cooled and dialyzed against ultrapure water using 10 kDa membranes (Spectra/Por$^{TM}$) until the conductivity fell below 5 μS cm$^{-1}$,[43] the resultant suspension was approximately pH 6. The DW Ge-INT suspension was recovered, and its mass concentration was determined by weight loss upon drying. The final concentration of DW Ge-INT suspension corresponds to an initial volume fraction (ϕ) 0.26%, a value close to 0.22% where a columnar phase was reported.[15] As-dialyzed DW Ge-INT aqueous suspensions were stored in air-tight vials to limit evaporation.

**Morphology Characterization of DW Ge-INTs**

The DW Ge-INTs synthesized had an average diameter of 4.3 ± 0.4 nm and average length of 85 ± 56 nm (statistics performed on 100 nanotubes observed by transmission electron microscopy), with very long aspect DW Ge-INTs also observed ca. 500 nm. Micrographs of synthesized DW Ge-INT can be found in the Figure S1. Transmission electron microscopy (TEM) images were taken using a JEOL-2010F Electron Microscope, JEOL Ltd, GB or on a JEOL1400 electron microscope operating at 80 kV. One drop of a dilute imogolite suspension (~1 mg L$^{-1}$) was deposited on a carbon-coated copper grid (lacey carbon films on 200 mesh, Agar Scientific, GB) lying on an absorbent paper and dried in air. Atomic force microscopy (AFM) micrographs were taken in tapping mode using a Digital Instruments Multimode VIII AFM with a Nano-scope IV controller. All AFM micrographs were recorded with a resolution of 512 lines and with a typical scanning speed of 1 Hz on prepared silicon substrates (Si wafer chips, Agar Scientific Ltd, GB), which were submerged in freshly prepared 3:1 mixture of $H_2SO_4$ (98%) and $H_2O_2$ (32%), before

washing with copious deionized water and drying at 120 °C. All micrographs were processed using NanoScope Analysis v1.40 (R2Sr), Bruker Corporation, US.

**Wet Spinning Production of DW Ge-INT/PVOH Fibers**

DW Ge-INT/PVOH dopant preparation: To make the initial dopant mixture, a PVOH in DMSO solution was made (105 °C, 4 h, 50 mg ml$^{-1}$) then deionized water added to maintain a fixed volume ratio of DMSO:water 4:1 (90 °C) prior to DW Ge-INT addition. As-dialyzed DW Ge-INT aqueous suspension was then slowly pipette dripped (9 mg ml$^{-1}$, 0.75 ml h$^{-1}$) into the PVOH/DMSO aqueous solution held at 90 °C under vigorous stirring (800 rpm) to produce the spinning dope. The concentration of DW Ge-INT in the dopant was varied by diluting the fixed volume of DW Ge-INT aqueous suspension added to the PVOH/DMSO/water solution.

Production of DW Ge-INT/PVOH composite fibers: The room temperature dope was collected into a 20 ml syringe and continuously injected through a 21-gauge (0.514 mm diameter) needle using a syringe pump (KDS 100, KDS Scientific Ltd, US) at 10 ml h$^{-1}$ into a rotating bath of antisolvent (acetone, between 20 and 25 °C) at an effective solution speed of 4.5 m min$^{-1}$ at injection point, to coagulate the composite fibers.[30]

As-spun fibers were then soaked in acetone (30 min) and transferred into a desiccator containing saturated ammonium sulfate solution and kept at 81% relative humidity until further processing. The DW Ge-INT/PVOH wet-spun composite fibers were then hot-drawn using a microfiber conditioning unit (DSM Xplore, Xplore Instruments BV, NL). The fibers were stretched under tension between two drum winders, with the initial winder speed set to 50 cm min$^{-1}$ and final 500 cm min$^{-1}$, whilst travelling through a split furnace (30 cm in length) operated at 180 °C, resulting in a constant draw ratio of 1:10 for all except for $\phi_{DW\ Ge-INT}$ = 13.2% which had a maximum attainable draw ratio of 1:5 (50 cm min$^{-1}$:250 cm min$^{-1}$). The total thread line torque

was maintained at 50 Nm. Nb. fibers were kept taut for 30 min to prevent contraction after hot-drawing. Further improvements to this system are anticipated, for example using longer or more monodispersed DW Ge-INTs, optimizing drawing conditions, as well as using an intrinsically more crystalline polymer (for example, PVOH with controlled tacticity).

**Characterization of DW Ge-INT/PVOH Composite Fibers**

Composite fiber morphology and composition: The morphology of the fibers was investigated by polarized optical microscope (DM2500P, Leica Microsystems Ltd., GB) fitted with a DFC295 camera (Leica Application Suite v4.0.0, $\infty$ /1.1 HI PLAN 40x/0.50) or on a BX51-P (Olympus Optical Co. Ltd., JP) equipped with a charge-coupled device camera, and through high resolution field emission gun SEM (LEO1525 Gemini, Carl Zeiss AG, CH) at an acceleration voltage of 5 kV at a working distance ca. 10 mm. The samples were coated with a 10 nm layer of Cr using a sputter coater (Q300T T, Quorum Technologies Ltd., GB), operating at a pressure of 70 mbar. All other SEM preparation supplies were bought from Agar Scientific, GB. The composition of the composite fiber cross section was probed using energy-dispersive X-ray (EDX) analysis in combination with SEM using INCA suite software V4.15, 2009, Oxford Instruments Plc., GB at an acceleration voltage of 10 kV.

Thermogravimetric analysis (TGA) was performed on a TGA/DSC 1 (Mettler-Toledo International Inc., CH), with a GC200 flow controller, using STARe software v12.00C. The samples were heated under nitrogen (60 sccm) from 30 °C to 100 °C at 35 °C min$^{-1}$, and then held isothermally at 100 °C for 30 min to dry, the temperature was then ramped to 750 °C at 10 ° C min$^{-1}$.

Crystallinity and alignment of PVOH and imogolite reinforcer in composite fibers: Differential scanning calorimetry (DSC 3, processed using STARe Software V.16.20, Mettler-

Toledo International Inc. CH) thermal analysis was conducted to determine the PVOH crystallinity in the drawn fibers. Fibers were collected into bundles of approximately 2 mg and placed into aluminum pans, which were analyzed in a nitrogen atmosphere. The samples were cycled twice from 35 ºC to 250 ºC at a heating rate and cooling rate of 10 ºC min$^{-1}$. Due to the similar melting and decomposition temperatures, the two endothermic peaks often overlapped. The melting and decomposition temperatures were nonetheless found to be approximately 225 ºC and 233 ºC respectively from samples with well-defined peaks. Overlapped peaks were thus deconvoluted by peak fitting a bi-Gaussian peak for melting and a Gaussian peak for decomposition around the two specified temperatures. All samples were visually inspected for decomposition after DSC experiments, which was indicated by a brown coloration. The melting peak areas were found by integrating the fitted bi-Gaussian peaks, and the melting enthalpy was compared to pure crystalline PVOH (156 J g$^{-1}$)[76] to determine the crystallinity of samples.

Wide angle X-ray scattering (WAXS) measurements were performed inside a vacuum chamber to avoid scattering by air. Measurements were carried out on a rotating anode (Model RU H3R, Rigaku Corporation, JP) using CuKα radiation ($\lambda$ = 0.154 nm) delivered by a multilayer W/Si optics. 2D scattering patterns were recorded on a MAR345 detector (marXperts GmbH, DE) perpendicular to the incident beam, placed at a distance of 148 mm from the fiber sample. For each measurement, the fiber was kept perpendicular to the incident X-ray beam. Linear scans were performed along two perpendicular translations of the scattering pattern corresponding to azimuthal angles $\tau$ = 0° (parallel to the fiber axis) and $\tau$ = 90° (perpendicular to fiber axis). In addition, angular profiles of scattered intensity were performed at constant $Q$ = 0.6 and 1.4 Å$^{-1}$, corresponding to scattering from the DW Ge-INTs in the plane $l$ = 0 and from PVOH.

Mechanical properties of DW Ge-INT/PVOH composite fibers: The mechanical response was observed under a tensile load following the standard BS ISO 11566:1996 adapted for use with composite/PVOH fibers and in conjunction with *in situ* video recording. Composite fibers were fixed on card frames with a gauge length $15 \pm 0.5$ mm using an epoxy adhesive (50/50 hardener to resin, Araldite Rapid Adhesive, Huntsman Advanced Materials Ltd., GB). Tensile tests of single composite fibers were carried out on TST350 tensile stress tester with integrated heating stage (Linkam Scientific Instruments Ltd., GB) with a 20 N load cell operating at 1 mm min$^{-1}$ crosshead speed at room temperature. At least ten samples were tested for each as-wet spun and drawn variation. The determination of average linear density in tex ($\delta_L$, 1 tex = 1 g km$^{-1}$ = 1 mg m$^{-1}$) was performed by measuring length and weight of the fiber samples by a ruler (over 600 mm to the nearest mm) and using a TGA/DSC 1LF/UMX Ultra Micro Balance (Mettler-Toledo International Inc., CH), respectively. The composite fiber's average tensile strength was calculated using $\delta_L/\delta_B$, where $\delta_L$ and $\delta_B$ are linear and bulk fiber densities, respectively. This method of determining fiber strength is classically carried out by the textile industry where natural fiber diameter variation can unduly influence strength appraisal. Subsequently, tex determined strengths provide a less bias evaluation than cross sectional area determined strengths. The bulk fiber density was calculated from the densities and volume fraction of each component amorphous PVOH (1.269 g cm$^{-3}$),[46] crystalline PVOH (1.345 g cm$^{-3}$),[46] and DW Ge-INT (3.6 g cm$^{-3}$ for determination see Supporting Information), excluding the contribution of any inter-particle void volume.

Evaporation induced self-assembly healing procedure for DW Ge-INT/PVOH composite fibers: Immediately after the first tensile failure of the specimen, the two fracture ends were returned to their initial extension in the tensile tester. The fiber fractures were often not clean breaks, allowing the two fractured surfaces to be returned parallel and adjacent to each other.

Evaporation induced self-assembly was performed using a droplet of water (200 mL) which was applied to the fractured region of the fiber ends and then heated to 95 °C for 10 min using the integrated heater until all the water had evaporated. For healed specimens, secondary tensile tests were conducted to determine the recovery strength and stiffness, following the previously described protocol. Mechanical properties of the healed fibers were determined using the as-spun linear density. This approach generates conservative values, ignoring any improvements in true strength and stiffness, due to the modest reduction in cross-section during the initial mechanical test, but is more relevant to the performance of healed structures. Healed composite fiber strains were measured from the onset load applied during the tensile test, with the gauge length defined, throughout, by the original gauge of the card frame support. Healing efficiencies ($\alpha$) were calculated using the following equations;

$$\alpha_E = \frac{E_{healed}}{E_{original}} \times 100 \ , \tag{1}$$

$$\alpha_\sigma = \frac{\sigma_{healed}}{\sigma_{original}} \times 100 \ , \tag{2}$$

where $E_{original}$, $E_{healed}$ is the tensile modulus of original and healed fibers, and $\sigma_{original}$, $\sigma_{healed}$ is the tensile strength of original and healed fibers, respectively. Healed fibers tensile properties were determined using the tex previously determined for the wet-spun and drawn fibers, with at least five healed specimens tested to provide average values. Not all of the original fibers were successfully healed due to difficulties in returning the fractured surfaces to be adjacent to one another in the tensile tester. A different camera was used to record the autonomic healing process, MG223B PoE E0022522 iMETRUM Ltd., GB using associated capture software v5.3.2, which was mounted directly to the DM2500P microscope's camera viewport, which is available in Supporting Video S1 (Nb. the video is sped up by x2).

## Author Information

### Author Contributions

W.J.L., P.L., and M.S.P.S. designed the study. E.P. synthesized the DW Ge-INTs. E.P. and S.R. carried out the WAXS experiments. P.L. and E.P. carried out the analysis of the X-ray scattering data. W.J.L., D.B.A., Y.G., and H.S.L. carried out the composite fiber fabrication and mechanical testing and other characterization detailed in the manuscript. W.J.L., E.P., and D.B.A. wrote the first version of the manuscript, and all authors participated in manuscript writing/editing and contributed to the data interpretation. All authors have given approval to the final version of the manuscript.

### ORCID

Won Jun Lee: 0000-0002-7121-057X

Erwan Paineau: 0000-0002-6776-7201

David Benbow Anthony: 0000-0002-4032-008X

Yulin Gao: 0000-0001-9335-1560

Hannah Siobhan Leese: 0000-0003-4523-3804

Pascale Launois: 0000-0003-4314-1076

Milo Sebastian Peter Shaffer: 0000-0001-9384-9043

## Associated Content

The authors declare no competing financial interest.

## Supporting Information

The Supporting Information contains figures and further discussions; including addition microscopy; Figure S1 TEM, and atomic force microscopy of DW Ge-INTs; Figure S2 optical/cross-polarized optical microscopy of DW Ge-INT suspensions; Figure S3 SEM of wet-spun fibers cryofractured cross-sections; Figure S6 cross-polarized optical microscopy of wet-spun fibers; and Figure S10 optical/cross-polarized optical microscopy of PVOH fiber after healing conditions. Thermal analysis of wet-spun fibers is shown in Figures S4, S5, and S7 corresponding to TGA thermographs, analysis of water uptake for wet-spun fibers, and DSC thermographs, respectively. Fiber composition, thermal, and morphological properties are tabulated in Table S1, and S2. Further discussion on the orientational order parameter determination for DW Ge-INTs and PVOH in wet-spun fibers are detailed with associated WAXS patterns (Figure S8) and scattering features tabulated in Table S3; and an estimation of the PVOH average crystallite size

compared to a commercial PVOH fiber, Figure S9 and Table S4. Mechanical data corresponding

to Figure 2(d) to (k) as-spun, and healed, is tabulated in Table S5, and S6, respectively. Additional

stress-strain plots for healed composite fibers is shown in Figure S11. Literature values used to

populate Figure 4 are tabulated in Table S7 and S8. An optical microscopy movie of DW Ge-

INT/PVOH composite fiber; tensile failure followed by evaporation induced self-assembly healing

procedure and second tensile test (AVI, Video S1). This material is available free of charge *via* the

Internet at http://pubs.acs.org.

## References

1.  Cook, J. G., *Introduction Fundamentals of Fibre Structure*. Woodhead Publishing: Cambridge, 2001; p 723, pp ix-xxx.
2.  Davis, V. A.; Parra-Vasquez, A. N. G.; Green, M. J.; Rai, P. K.; Behabtu, N.; Prieto, V.; Booker, R. D.; Schmidt, J.; Kesselman, E.; Zhou, W.; Fan, H.; Adams, W. W.; Hauge, R. H.; Fischer, J. E.; Cohen, Y.; Talmon, Y.; Smalley, R. E.; Pasquali, M., True Solutions of Single-Walled Carbon Nanotubes for Assembly into Macroscopic Materials. *Nat. Nanotechnol.* **2009,** *4*, 830-834.
3.  Song, K.; Zhang, Y.; Meng, J.; Green, E.; Tajaddod, N.; Li, H.; Minus, M., Structural Polymer-Based Carbon Nanotube Composite Fibers: Understanding the Processing–Structure–Performance Relationship. *Materials* **2013,** *6,* 2543.
4.  Li, Y.-L.; Kinloch, I. A.; Windle, A. H., Direct Spinning of Carbon Nanotube Fibers from Chemical Vapor Deposition Synthesis. *Science* **2004,** *304*, 276-278.
5.  Vigolo, B.; Pénicaud, A.; Coulon, C.; Sauder, C.; Pailler, R.; Journet, C.; Bernier, P.; Poulin, P., Macroscopic Fibers and Ribbons of Oriented Carbon Nanotubes. *Science* **2000,** *290*, 1331-1334.
6.  Moulton, S. E.; Maugey, M.; Poulin, P.; Wallace, G. G., Liquid Crystal Behavior of Single-Walled Carbon Nanotubes Dispersed in Biological Hyaluronic Acid Solutions. *JACS* **2007,** *129*, 9452-9457.
7.  Behabtu, N.; Young, C. C.; Tsentalovich, D. E.; Kleinerman, O.; Wang, X.; Ma, A. W. K.; Bengio, E. A.; ter Waarbeek, R. F.; de Jong, J. J.; Hoogerwerf, R. E.; Fairchild, S. B.; Ferguson, J. B.; Maruyama, B.; Kono, J.; Talmon, Y.; Cohen, Y.; Otto, M. J.; Pasquali, M., Strong, Light, Multifunctional Fibers of Carbon Nanotubes with Ultrahigh Conductivity. *Science* **2013,** *339*, 182-186.
8.  de Gennes, P.-G.; Prost, J., *The Physics of Liquid Crystals* Second Editions ed.; Clarendon Press: Oxford, 1993; p 616, pp 2.
9.  Livolant, F.; Levelut, A. M.; Doucet, J.; Benoit, J. P., The Highly Concentrated Liquid-Crystalline Phase of DNA is Columnar Hexagonal. *Nature* **1989,** *339*, 724-726.
10. Grelet, E., Hexagonal Order in Crystalline and Columnar Phases of Hard Rods. *Phys. Rev. Lett.* **2008,** *100,* 168301.

11. Kato, T., Self-Assembly of Phase-Segregated Liquid Crystal Structures. *Science* **2002,** *295*, 2414-2418.
12. Bong, D. T.; Clark, T. D.; Granja, J. R.; Ghadiri, M. R., Self-Assembling Organic Nanotubes. *Angew. Chem. Int. Ed.* **2001,** *40*, 988-1011.
13. Amara, M.-S.; Paineau, E.; Bacia-Verloop, M.; Krapf, M.-E. M.; Davidson, P.; Belloni, L.; Levard, C.; Rose, J.; Launois, P.; Thill, A., Single-Step Formation of Micron Long $(OH)_3Al_2O_3Ge(OH)$ Imogolite-Like Nanotubes. *Chem. Commun.* **2013,** *49*, 11284-11286.
14. Ni, B.; Liu, H.; Wang, P.-p.; He, J.; Wang, X., General Synthesis of Inorganic Single-Walled Nanotubes. *Nat. Commun.* **2015,** *6*, 8756.
15. Paineau, E.; Krapf, M.-E. M.; Amara, M.-S.; Matskova, N. V.; Dozov, I.; Rouzière, S.; Thill, A.; Launois, P.; Davidson, P., A Liquid-Crystalline Hexagonal Columnar Phase in Highly-Dilute Suspensions of Imogolite Nanotubes. *Nat. Commun.* **2016,** *7*, 10271.
16. Cradwick, P. D. G.; Farmer, V. C.; Russell, J. D.; Masson, C. R.; Wada, K.; Yoshinaga, N., Imogolite, A Hydrated Aluminium Silicate of Tubular Structure. *Nature (London), Phys. Sci.* **1972,** *240*, 187-189.
17. Guimarães, L.; Enyashin, A. N.; Frenzel, J.; Heine, T.; Duarte, H. A.; Seifert, G., Imogolite Nanotubes: Stability, Electronic, and Mechanical Properties. *ACS Nano* **2007,** *1*, 362-368.
18. Monet, G.; Amara, M. S.; Rouzière, S.; Paineau, E.; Chai, Z.; Elliott, J. D.; Poli, E.; Liu, L.-M.; Teobaldi, G.; Launois, P., Structural Resolution of Inorganic Nanotubes with Complex Stoichiometry. *Nat. Commun.* **2018,** *9*, 2033.
19. Levard, C.; Basile-Doelsch, I., Chapter 3 - Geology and Mineralogy of Imogolite-Type Materials. In *Developments in Clay Science*, Yuan, P.; Thill, A.; Bergaya, F., Eds. Elsevier: Amsterdam, 2016; Vol. 7, pp 49-65.
20. Shikinaka, K., Design of Stimuli-Responsive Materials Consisting of the Rigid Cylindrical Inorganic Polymer `Imogolite'. *Polym. J.* **2016,** *48*, 689-696.
21. Ryu, J.; Ko, J.; Lee, H.; Shin, T.-G.; Sohn, D., Structural Response of Imogolite–Poly(Acrylic Acid) Hydrogel under Deformation. *Macromolecules* **2016,** *49*, 1873-1881.
22. Lourenço, M. P.; Guimarães, L.; da Silva, M. C.; de Oliveira, C.; Heine, T.; Duarte, H. A., Nanotubes with Well-Defined Structure: Single- and Double-Walled Imogolites. *J. Phys. Chem. C* **2014,** *118*, 5945-5953.
23. Yah, W. O.; Yamamoto, K.; Jiravanichanun, N.; Otsuka, H.; Takahara, A., Imogolite Reinforced Nanocomposites: Multifaceted Green Materials. *Materials* **2010,** *3*, 1709.
24. Ma, W.; Yah, W. O.; Otsuka, H.; Takahara, A., Application of Imogolite Clay Nanotubes in Organic–Inorganic Nanohybrid Materials. *J. Mater. Chem.* **2012,** *22*, 11887-11892.
25. Hyun, C. J.; Woo, C. Y.; Shik, H. W.; Seok, L. W.; Joo, L. C.; Chul, J. B.; Soo, H. S.; Shik, Y. W., Preparation and Characterization of Syndiotacticity-Rich Ultra-High Molecular Weight Poly(Vinyl Alcohol)/Imogolite Blend Film. *Polym. Int.* **1998,** *47*, 237-242.
26. Paineau, E., Imogolite Nanotubes: A Flexible Nanoplatform with Multipurpose Applications. *Appl. Sci.* **2018,** *8*, 1921.
27. Davidson, P.; Dozov, I., Chapter 13 - Liquid-Crystalline Phases of Imogolite and Halloysite Dispersions. In *Developments in Clay Science*, Yuan, P.; Thill, A.; Bergaya, F., Eds. Elsevier: Amsterdam, 2016; Vol. 7, pp 308-330.
28. Su, C.-Y.; Yang, A.-C.; Jiang, J.-S.; Yang, Z.-H.; Huang, Y.-S.; Kang, D.-Y.; Hua, C.-C., Properties of Single-Walled Aluminosilicate Nanotube/Poly(Vinyl Alcohol) Aqueous Dispersions. *J. Phys. Chem. B* **2018,** *122*, 380-391.

29. Coleman, J. N.; Cadek, M.; Ryan, K. P.; Fonseca, A.; Nagy, J. B.; Blau, W. J.; Ferreira, M. S., Reinforcement of Polymers with Carbon Nanotubes. The Role of an Ordered polymer Interfacial Region. Experiment and Modeling. *Polymer* **2006,** *47*, 8556-8561.

30. Lee, W. J.; Clancy, A. J.; Kontturi, E.; Bismarck, A.; Shaffer, M. S. P., Strong and Stiff: High-Performance Cellulose Nanocrystal/Poly(Vinyl Alcohol) Composite Fibers. *ACS Appl. Mater. Interfaces* **2016,** *8*, 31500-31504.

31. Mercader, C.; Denis-Lutard, V.; Jestin, S.; Maugey, M.; Derré, A.; Zakri, C.; Poulin, P., Scalable Process for the Spinning of PVA–Carbon Nanotube Composite Fibers. *J. Appl. Polym. Sci.* **2012,** *125*, E191-E196.

32. Miaudet, P.; Badaire, S.; Maugey, M.; Derré, A.; Pichot, V.; Launois, P.; Poulin, P.; Zakri, C., Hot-Drawing of Single and Multiwall Carbon Nanotube Fibers for High Toughness and Alignment. *Nano Lett.* **2005,** *5*, 2212-2215.

33. Hoshino, H.; Ito, T.; Donkai, N.; Urakawa, H.; Kajiwara, K., Lyotropic Mesophase Formation in PVA/Imogolite Mixture. *Polym. Bull.* **1992,** *29*, 453-460.

34. Ajayan, P. M.; Tour, J. M., Materials Science: Nanotube Composites. *Nature* **2007,** *447*, 1066-1068.

35. Nagara, Y.; Nakano, T.; Okamoto, Y.; Gotoh, Y.; Nagura, M., Properties of Highly Syndiotactic Poly(Vinyl Alcohol). *Polymer* **2001,** *42*, 9679-9686.

36. Sakurada, I.; Okaya, T., *Handbook of Fiber Chemistry*. Third Edition ed.; CRC Press: Boca Raton, 2006; p 1056, pp 265.

37. Schellekens, R.; Bastiaansen, C., The Drawing Behavior of Polyvinylalcohol Fibers. *J. Appl. Polym. Sci.* **1991,** *43*, 2311-2315.

38. Li, L.; Li, B.; Hood, M. A.; Li, C. Y., Carbon Nanotube Induced Polymer Crystallization: The Formation of Nanohybrid Shish–Kebabs. *Polymer* **2009,** *50*, 953-965.

39. Lee, W. J.; Clancy, A. J.; Fernández-Toribio, J. C.; Anthony, D. B.; White, E. R.; Solano, E.; Leese, H. S.; Vilatela, J. J.; Shaffer, M. S. P., Interfacially-Grafted Single-Walled Carbon Nanotube / Poly (Vinyl Alcohol) Composite Fibers. *Carbon* **2019,** *146*, 162-171.

40. Bunn, C. W., Crystal Structure of Polyvinyl Alcohol. *Nature* **1948,** *161*, 929.

41. Tache, O.; Rouziere, S.; Joly, P.; Amara, M.; Fleury, B.; Thill, A.; Launois, P.; Spalla, O.; Abecassis, B., MOMAC: A SAXS/WAXS Laboratory Instrument Dedicated to Nanomaterials. *J. Appl. Crystallogr.* **2016,** *49*, 1624-1631.

42. Amara, M. S.; Rouzière, S.; Paineau, E.; Bacia-Verloop, M.; Thill, A.; Launois, P., Hexagonalization of Aluminogermanate Imogolite Nanotubes Organized into Closed-Packed Bundles. *J. Phys. Chem. C* **2014,** *118*, 9299-9306.

43. Paineau, E.; Amara, M. S.; Monet, G.; Peyre, V.; Rouzière, S.; Launois, P., Effect of Ionic Strength on the Bundling of Metal Oxide Imogolite Nanotubes. *J. Phys. Chem. C* **2017,** *121*, 21740-21749.

44. Assender, H. E.; Windle, A. H., Crystallinity in Poly(Vinyl Alcohol). 1. An X-Ray Diffraction Study of Atactic PVOH. *Polymer* **1998,** *39*, 4295-4302.

45. Pichot, V.; Badaire, S.; Albouy, P. A.; Zakri, C.; Poulin, P.; Launois, P., Structural and Mechanical Properties of Single-Wall Carbon Nanotube Fibers. *Phys. Rev. B* **2006,** *74*, 245416.

46. Peppas, N. A.; Merrill, E. W., Poly(Vinyl Alcohol) Hydrogels: Reinforcement of Radiation-Crosslinked Networks by Crystallization. *J. Polym. Sci., Part A: Polym. Chem.* **1976,** *14*, 441-457.

47. Phadke, A.; Zhang, C.; Arman, B.; Hsu, C.-C.; Mashelkar, R. A.; Lele, A. K.; Tauber, M. J.; Arya, G.; Varghese, S., Rapid Self-Healing Hydrogels. *Proc. Natl. Acad. Sci. U. S. A.* **2012,** *109*, 4383-4388.

48. Li, C.-H.; Wang, C.; Keplinger, C.; Zuo, J.-L.; Jin, L.; Sun, Y.; Zheng, P.; Cao, Y.; Lissel, F.; Linder, C.; You, X.-Z.; Bao, Z., A Highly Stretchable Autonomous Self-Healing Elastomer. *Nat. Chem.* **2016,** *8*, 618-624.

49. Chen, Y.; Kushner, A. M.; Williams, G. A.; Guan, Z., Multiphase Design of Autonomic Self-Healing Thermoplastic Elastomers. *Nat. Chem.* **2012,** *4*, 467-472.

50. Wang, Y.; Pham, D. T.; Ji, C., Self-Healing Composites: A Review. *Cogent Engineering* **2015,** *2*, 1075686.

51. Cohades, A.; Branfoot, C.; Rae, S.; Bond, I.; Michaud, V., Progress in Self-Healing Fiber-Reinforced Polymer Composites. *Adv. Mater. Interfaces* **2018,** *5*, 1800177.

52. Dalton, A. B.; Collins, S.; Munoz, E.; Razal, J. M.; Ebron, V. H.; Ferraris, J. P.; Coleman, J. N.; Kim, B. G.; Baughman, R. H., Super-Tough Carbon-Nanotube Fibres. *Nature* **2003,** *423*, 703-703.

53. Simmons, A. H.; Michal, C. A.; Jelinski, L. W., Molecular Orientation and Two-Component Nature of The Crystalline Fraction of Spider Dragline Silk. *Science* **1996,** *271*, 84-87.

54. Yoshino, T.; Kondo, M.; Mamiya, J.-i.; Kinoshita, M.; Yu, Y.; Ikeda, T., Three-Dimensional Photomobility of Crosslinked Azobenzene Liquid-Crystalline Polymer Fibers. *Adv. Mater.* **2010,** *22*, 1361-1363.

55. Blaiszik, B. J.; Kramer, S. L. B.; Olugebefola, S. C.; Moore, J. S.; Sottos, N. R.; White, S. R., Self-Healing Polymers and Composites. *Annu. Rev. Mater. Res.* **2010,** *40*, 179-211.

56. Huang, Y.; Huang, Y.; Zhu, M.; Meng, W.; Pei, Z.; Liu, C.; Hu, H.; Zhi, C., Magnetic-Assisted, Self-Healable, Yarn-Based Supercapacitor. *ACS Nano* **2015,** *9*, 6242-6251.

57. Ariga, K.; Mori, T.; Hill, J. P., Mechanical Control of Nanomaterials and Nanosystems. *Adv. Mater.* **2012,** *24*, 158-176.

58. D'Elia, E.; Eslava, S.; Miranda, M.; Georgiou, T. K.; Saiz, E., Autonomous Self-Healing Structural Composites with Bio-Inspired Design. *Sci. Rep.* **2016,** *6*, 25059.

59. Agrawal, A.; Chipara, A. C.; Shamoo, Y.; Patra, P. K.; Carey, B. J.; Ajayan, P. M.; Chapman, W. G.; Verduzco, R., Dynamic Self-Stiffening in Liquid Crystal Elastomers. *Nat. Commun.* **2013,** *4*, 1739.

60. Castellano, R. K.; Nuckolls, C.; Eichhorn, S. H.; Wood, M. R.; Lovinger, A. J.; Rebek, J. J., Hierarchy of Order in Liquid Crystalline Polycaps. *Angew. Chem. Int. Ed.* **1999,** *38*, 2603-2606.

61. Jeffrey, B. C.; Yunfeng, L.; Alan, S.; Hongyou, F., Evaporation-Induced Self-Assembly: Nanostructures Made Easy. *Adv. Mater.* **1999,** *11*, 579-585.

62. Li, S.-J.; Qian, H.-J.; Lu, Z.-Y., Translational and Rotational Dynamics of an Ultra-Thin Nanorod Probe Particle in Linear Polymer Melts. *Phys. Chem. Chem. Phys.* **2018,** *20*, 20996-21007.

63. Plaisted, T. A.; Nemat-Nasser, S., Quantitative Evaluation of Fracture, Healing and Re-Healing of a Reversibly Cross-Linked Polymer. *Acta Mater.* **2007,** *55*, 5684-5696.

64. Luterbacher, R.; Coope, T. S.; Trask, R. S.; Bond, I. P., Vascular Self-Healing within Carbon Fibre Reinforced Polymer Stringer Run-Out Configurations. *Compos. Sci. Technol.* **2016,** *136*, 67-75.

65. Zechel, S.; Geitner, R.; Abend, M.; Siegmann, M.; Enke, M.; Kuhl, N.; Klein, M.; Vitz, J.; Gräfe, S.; Dietzek, B.; Schmitt, M.; Popp, J.; Schubert, U. S.; Hager, M. D., Intrinsic Self-

Healing Polymers with a High E-Modulus Based on Dynamic Reversible Urea Bonds. *NPG Asia Mater.* **2017,** *9*, e420.

66. Archer, E.; McIlhagger, A., 14 - Repair of Damaged Aerospace Composite Structures. In *Polymer Composites in the Aerospace Industry*, Irving, P. E.; Soutis, C., Eds. Woodhead Publishing: Amsterdam, 2015; pp 393-412.

67. Ashby, M. F., *Materials Selection in Mechanical Design*. 4th ed.; Butterworth-Heinemann: Cambridge, 2011; p 640, pp 57-96.

68. White, S. R.; Sottos, N. R.; Geubelle, P. H.; Moore, J. S.; Kessler, M. R.; Sriram, S. R.; Brown, E. N.; Viswanathan, S., Autonomic Healing of Polymer Composites. *Nature* **2001,** *409*, 794-797.

69. Hager, M. D.; Greil, P.; Leyens, C.; van der Zwaag, S.; Schubert, U. S., Self-Healing Materials. *Adv. Mater.* **2010,** *22*, 5424-5430.

70. Murphy, E. B.; Wudl, F., The World of Smart Healable Materials. *Prog. Polym. Sci.* **2010,** *35*, 223-251.

71. Balazs, A. C., Modeling Self-Healing Materials. *Mater. Today* **2007,** *10*, 18-23.

72. Ma, W.; Otsuka, H.; Takahara, A., Poly(Methyl Methacrylate) Grafted Imogolite Nanotubes Prepared through Surface-Initiated ARGET ATRP. *Chem. Commun.* **2011,** *47*, 5813-5815.

73. Shikinaka, K.; Abe, A.; Shigehara, K., Nanohybrid Film Consisted of Hydrophobized Imogolite and Various Aliphatic Polyesters. *Polymer* **2015,** *68*, 279-283.

74. Luo, Z.; Song, H.; Feng, X.; Run, M.; Cui, H.; Wu, L.; Gao, J.; Wang, Z., Liquid Crystalline Phase Behavior and Sol–Gel Transition in Aqueous Halloysite Nanotube Dispersions. *Langmuir* **2013,** *29*, 12358-12366.

75. Ma, W.; Wu, H.; Higaki, Y.; Takahara, A., Halloysite Nanotubes: Green Nanomaterial for Functional Organic-Inorganic Nanohybrids. *Chem. Rec.* **2018,** *18*, 986-999.

76. Tubbs, R. K., Melting Point and Heat of Fusion of Poly(Vinyl Alcohol). *J. Polym. Sci., Part A: Gen. Pap.* **1965,** *3*, 4181-4189.

**Table of Contents Graphic**